arXiv:2008.04337v1 [cond-mat.str-el] 10 Aug 2020

A Striped Electron Fluid on (111) $KTaO_3$

P. Villar Arribi,[1] A. Paramekanti,[2] and M. R. Norman[1]

[1] *Materials Science Division, Argonne National Laboratory, Lemont, IL 60439, USA*
[2] *Department of Physics, University of Toronto, Toronto, Ontario M5S1A7, Canada.*

(Dated: February 2, 2022)

A recent study has revealed that the low carrier density electron gas (2DEG) induced at the interface of EuO and (111) $KTaO_3$ exhibits a broken symmetry phase with a strong in-plane anisotropy of the resistivity. We present a minimal tight binding model of this (111) 2DEG, including the large spin-orbit coupling from the Ta ions, which reveals a hexagonal Fermi surface with a highly enhanced $2k_F$ electronic susceptibility. We argue that repulsive electronic interactions, together with a ferromagnetic EuO substrate, favor a magnetic stripe instability leading to a partially gapped Fermi surface. Such a stripe state, or its vestigial nematicity, could explain the observed transport anisotropy. We propose a $k \cdot p$ theory for the low energy $j = 3/2$ states, which captures the key results from our tight-binding study, and further reveals the intertwined dipolar and octupolar modulations underlying this magnetic stripe order. We conclude by speculating on the relation of this stripe order to the superconductivity seen in this material.

The superconducting 2DEG at the surface of $SrTiO_3$ has been the subject of much investigation since its observation back in 2007 [1]. A few years later, its $5d$ analog, $KTaO_3$ (KTO), was found to exhibit superconductivity (SC) at 50 mK in an (001) 2DEG created using ionic liquid gating [2]. A recent experiment discovered that for (111) oriented KTO, T_c is dramatically enhanced, by a factor of 40, with SC occurring up to $\sim$2 K at carrier densities $n \sim 10^{14}/\text{cm}^2$ [3]. Even more remarkably, at low carrier densities where SC occurs with $T_c \sim 0.5$ K, it descends from an apparent nematic phase with a significant in-plane resistance anisotropy of $\sim$3 [3]. This anisotropy onsets abruptly at a higher temperature 2.2 K, suggesting a phase transition into an ordered state. At zero magnetic field, the anisotropy is only observed if KTO is in contact with EuO (for KTO on $LaAlO_3$, an in-plane magnetic field is required for its observation [3]). As EuO is ferromagnetic, magnetism is likely to play an important role in this phenomenon. The presence of charge, spin, and superconducting correlations as a function of carrier concentration for (111) KTO is reminiscent of a number of other materials such as cuprates [4, 5], iron pnictides and chalcogenides [6], doped Bi_2Se_3 [7–9], and twisted bilayer graphene near a magic angle [10]. Furthermore, since the conduction band of KTO arises from spin-orbit coupled (SOC) $j = 3/2$ states [11, 12], the broken symmetry nematic is expected to also display intertwined multipolar orders as conjectured for $Cd_2Re_2O_7$ [13–16].

KTO is a band insulator with a large gap $\sim$ 3.6 eV [17]. Experiments have realized both a (001) 2DEG [3, 18–21] and a (111) 2DEG [3, 12, 22] at the free surface of KTO, due to oxygen vacancies induced by cleaving or by irradiating the surface, as well as at KTO interfaces with oxides such as $LaAlO_3$ and EuO. Fig. 6 shows the crystal structure of (111) KTO, consisting of alternating layers of Ta and KO_3, with each Ta layer forming a triangular lattice. This structure is highly polar given the 5+ nature of the Ta ions. Angle resolved photoemission spectroscopy

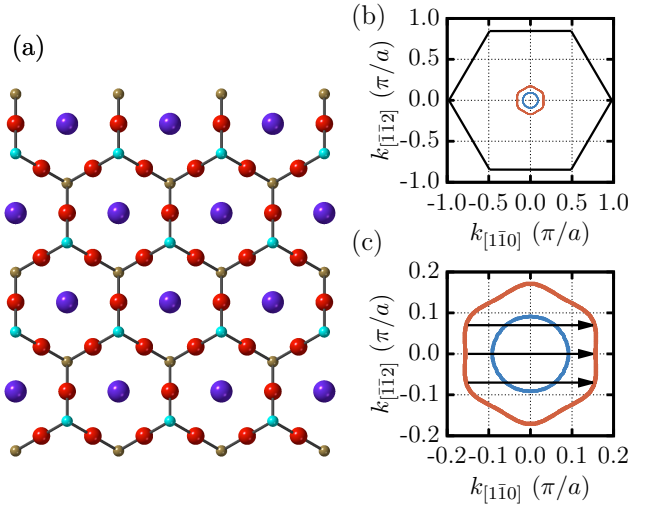


FIG. 1. (a) Crystal structure of the top three (111) layers of KTO (Ta, KO_3, Ta), with the horizontal axis along (1,-1,0) and the vertical axis along (1,1,-2). K ions are in purple, O ions in red, Ta ions in the top layer in cyan and Ta ions in the bottom layer in gold. (b) Fermi surface of (111) KTO from the bilayer tight-binding model and the carrier density of the nematic state. (c) Blow up of (b), showing the nesting wavevectors associated with the outer sheet of the Fermi surface. a refers to the cubic lattice constant of KTO.

(ARPES) of the 2DEG revealed six-fold symmetric Fermi surfaces (FSs) [12, 22]. The observed bands were found to be captured by a (111) bilayer model [22], consisting of t_{2g} orbitals from two Ta layers forming a buckled honeycomb plane, a setting proposed for realizing topological phases by Xiao *et al.* [23].

We find that a minimal two-parameter honeycomb tight-binding model provides a good description of the ARPES observations; details can be found in [24] and Refs. [3, 12, 23, 25]. The dominant scale is the Ta-O-Ta hopping, $t \sim 1$ eV, which is proportional to t_{pd}^2/Δ_{pd}

where t_{pd} is the hopping between the Ta $5d$ t_{2g} and O $2p$ orbitals, and Δ_{pd} is the Ta-O charge transfer energy. Since each Ta t_{2g} orbital hops to only two of the three nearest neighbors on the honeycomb lattice, the resulting bands exhibit 1D character. The FS of each orbital forms a spin-degenerate pair of parallel lines, with the FS of different orbitals rotated with respect to each other by 120 degrees [24]. The inclusion of SOC, $\lambda \sim 0.25\,\text{eV}$, which is the next largest energy scale, dramatically alters the electronic structure. SOC hybridizes the different 1D dispersions, and splits the t_{2g} manifold at the Γ-point into a lower $j=3/2$ quartet and an upper $j=1/2$ doublet, separated by $\sim 0.4\,\text{eV}$. The net result is that the parallel FS lines break up and reconstruct into closed FSs. Motivated by Ref. 12, we supplement this minimal model with a small trigonal distortion term so the $j=3/2$ quartet at Γ splits into two Kramers doublets separated by $\sim 15\,\text{meV}$. Our model provides a reasonable description of the recent ARPES data [12, 24], at a density $n \sim 10^{14}/\text{cm}^2$, which reveals a larger outer star-shaped FS along with an inner hexagonal FS, both centered at Γ [26].

The recent experiments which observe nematic transport correspond to lower densities $n \sim 3.5 \times 10^{13}/\text{cm}^2$. To explore this regime, we start from our well-motivated model above, and lower the chemical potential to achieve this density. The resulting FS, shown in Fig. 6, reveals an inner circular FS, and an outer hexagonal FS which has flat faces nested along the Γ-K directions. We examine below the consequences of this nesting for $2k_F$ stripe order and transport anisotropy. The FSs shown in Fig. 6 are spin-degenerate; we later incorporate weak Rashba spin splitting [12, 22] induced by the broken inversion symmetry at the interface.

The susceptibility for such a hexagonal FS is expected to resemble the 1D Lindhard function which diverges logarithmically in T at the nesting wavevector. Interestingly, the nesting direction is along Γ-K (i.e., the (1,-1,0) direction) which corresponds precisely to the observed high resistivity direction in the nematic phase [3]. In a stripe model for the nematic phase, one would indeed anticipate that the resistivity is maximal along the stripe wavevector, $\mathbf{q}_s$. To investigate this further, we calculate the Lindhard susceptibility, χ_0, for the bilayer model:

$$\chi_0(\mathbf{q}) = \sum_{\mathbf{k},n,m} \frac{f_{\mathbf{k},n} - f_{\mathbf{k}+\mathbf{q},m}}{\epsilon_{\mathbf{k}+\mathbf{q},m} - \epsilon_{\mathbf{k},n} + i\delta} \qquad (1)$$

where m and n are band indices, f are Fermi functions, ϵ are the band energies, and δ is a small broadening (set to 0.1 meV or smaller). Although the bilayer model has six spin-degenerate pairs of bands (three t_{2g} orbitals, two layers), only the lowest two are relevant at low energy and we confine our discussion to them. To begin with, we will be agnostic concerning spin versus charge, and therefore not include matrix elements until later. The resulting χ_0, decomposed in terms of n and m, is shown in Fig. 2a. As

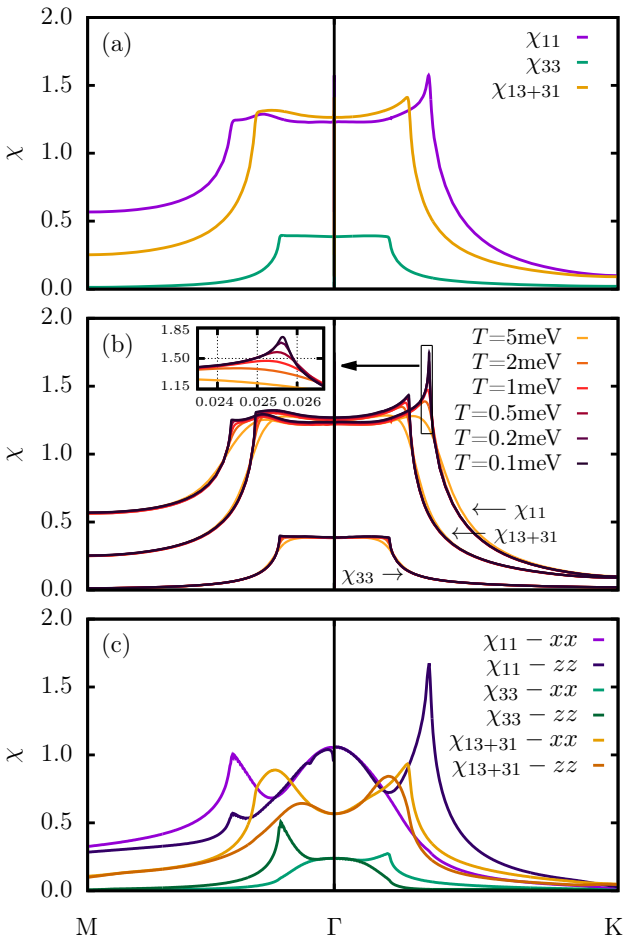


FIG. 2. (a) Lindhard susceptibility, χ_0, along Γ-M and Γ-K computed with $T = 0.5$ meV. Subscripts 1, 3 are band indices (1 for the outer FS, 3 for the inner FS, noting that bands 1,2 and 3,4 are Kramers degenerate). (b) Evolution of the susceptibility with temperature. Inset: detail of the cusp in χ_{11} along the Γ-K direction associated with the outer FS. (c) Lindhard susceptibility including spin matrix elements as defined in Eq. 2. x and z correspond to the spin operators S_x and S_z. The strong (11) cusp is only found for the zz component.

expected, the outer hexagon gives rise to a susceptibility maximum along Γ-K due to nesting of each of the two parallel sides of the hexagon (as indicated in Fig. 6c). This is evident from the cusp-like behavior of the intraband χ_0, indicating quasi-1D behavior. Fig. 2b shows that this cusp becomes better defined upon lowering T, as expected.

To proceed further, we need to consider matrix elements. In the experiments, the nematic phase at zero magnetic field is found at the KTO-EuO interface, but not at the KTO-$LaAlO_3$ interface. This indicates that magnetism is playing a key role. This can be understood from the fact that the Eu $4f$ electrons exhibit ferromagnetic order with a large moment. These $4f$ electrons

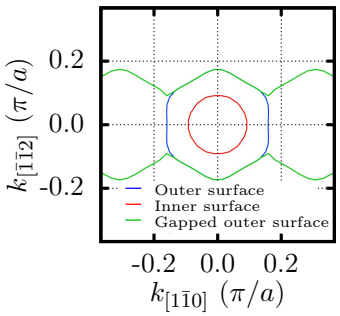


FIG. 3. Original FS from Fig. 6 (red,blue), as well as the reconstructed outer FS (green) due to a spin density wave potential, $V(\mathbf{q}_s)$, of strength 4.4 K, with $\mathbf{q}_s = (q_s, 0)$ and q_s given by the peak in χ_0 along Γ-K for the outer FS.

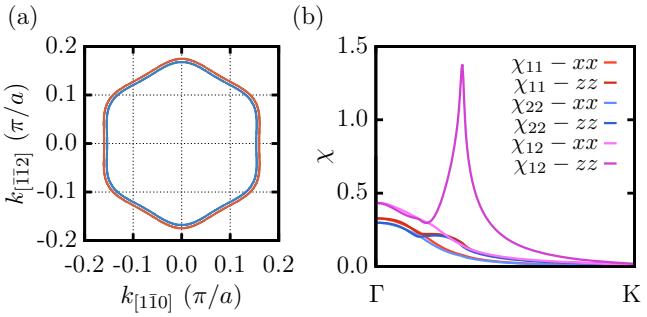


FIG. 4. (a) Outer FS as in Fig. 6c, but including a Rashba term which lifts the Kramers degeneracy. (b) Resulting Lindhard susceptibility, χ_0, computed with $T = 0.5$ meV, including spin matrix elements as defined in Eq. 2 plotted along the (1,-1,0) direction. The cusp is again associated with the zz component, but now is an interband term between the two Rashba-split bands.

overlap with the Eu 5d orbitals which in turn overlap with the Ta 5d electrons (the Ta to oxide layer spacing in (111) KTO is only 1.15 Å, whereas $\langle r \rangle_{\mathrm{Eu}-4f} \sim 0.9$Å, $\langle r \rangle_{\mathrm{Eu}-5d} \sim 2.7$ Å, and $\langle r \rangle_{\mathrm{Ta}-5d} \sim 2.2$ Å [27]). Calculations for (001) EuO-KTO find induced moments of $\sim 0.2\ \mu_B$ on the first TaO_2 layer [28]. This motivates including spin matrix elements in the numerator of Eq. 1:

$$g^2 \langle \mathbf{k}, n| S_i(\mathbf{q}) |\mathbf{k}+\mathbf{q}, m\rangle \langle \mathbf{k}+\mathbf{q}, m| S_j(\mathbf{q}) |\mathbf{k}, n\rangle \qquad (2)$$

where $g = 2$, S_i are spin-$\frac{1}{2}$ operators (i=x, y, z), and $|\mathbf{k}, n\rangle$ are the band eigenvectors. Because of strong SOC, the susceptibility is anisotropic even without the feedback from the energy gap due to density wave formation. The results are shown in Fig. 2c. The cusp along Γ-K is associated with the zz component of χ. As z is orthogonal to (1,-1,0), this implies a transverse spin density wave, which is typical for a magnetic stripe model [29].

The mean field transition temperature is determined by the divergence of the full interacting susceptibility. This is given by the condition $I(\mathbf{q})\chi_0(\mathbf{q}, T) = 1$, where $I(\mathbf{q})$ is the interaction function. Based on the above considerations, we expect $I(\mathbf{q})$ would be induced by the combined effect of the amorphous ferromagnetic EuO substrate and local Ta correlations, rendering it a weak function of $\mathbf{q}$. Thus, the ordering vector would be determined by the cusp in χ_0. The value of $I(\mathbf{q})$ would need to be sizable (on the scale of ~ 1 eV) in order to induce the transition, with the low value of T_s due to the logarithmic (BCS-like) rise in the cusp of χ_0 with decreasing T as can be seen in Fig. 2b. In this scenario, the disappearance of nematicity in higher carrier density samples could be due to the reduction of $I(\mathbf{q})$ from screening, or due to enhanced disorder scattering as reflected by the lower mobility of such samples [3].

We next consider the question of transport anisotropy in this stripe state. In Fig. 9, we show the outer FS as reconstructed by a spin-density wave within a simple calculation [30] involving a 3×3 secular matrix where one couples the states $\mathbf{k} - \mathbf{q}_s$ and $\mathbf{k} + \mathbf{q}_s$ with $\mathbf{k}$, with $\mathbf{k}$ from the lowest band (band 1) and a stripe potential, $V(\mathbf{q}_s)$. Here, we take $\mathbf{q}_s = (q_s, 0)$, and $V(\mathbf{q}_s)$ to have a typical mean-field value of $2T_s$ where $T_s \sim 2.2$ K from Ref. 3. We find that the original FS is wiped out along the nesting direction, leading to a reconstructed open FS which is expected to exhibit a strong resistive anisotropy.

We briefly comment on the energetic competition between a single-**q** state versus a triple-**q** state. In the presence of SOC, for a fixed spin direction, only one of the three equivalent Γ-K directions would have a cusp, but not the other two (as in Fig. 2c), leading to transport nematicity. Based on the above FS reconstruction, one might expect that a triple-**q** state would gap out the entire outer FS (i.e., all hexagonal faces), and thus would be energetically preferred over the single-**q** one. Such a state would not have an in-plane transport anisotropy. However, such non-coplanar spin crystals typically arise for a non-zero perpendicular magnetization whereas the EuO magnetization is expected to be in the plane of the interface. In this case, SOC could favor the single-**q** state, with the moment direction locked to the stripe wavevector. This provides further support of a magnetic stripe rather than a charge stripe order. A complete treatment of this problem would require calculating the cubic and quartic terms in a Landau free-energy expansion [31, 32], but this time including the spin matrix elements. This is an involved task, which we defer to future work.

We next consider the effect of the Rashba spin splitting. In a single-layer model, the Rashba term for the (111) case is given in Ref. 33. As the Ta-Ta hopping in-plane is weak, we instead consider the Rashba term given by the Ta-O-Ta path connecting the layers, which is a (111) generalization of the (001) case considered by Khalsa *et al.* [25]. Here, the largest term is due to inversion breaking on one of the Ta-O segments followed by a t_{pd} hop along the other. The functional form is given

in [24]. Both this form and the one of Ref. 33, which are off-diagonal in the orbital index, give similar results, with a relatively isotropic Rashba splitting around the FS (Fig. 8a). The effect of this is minor for χ_0 without matrix elements given the small value of the Rashba splitting (of order a few meV). However, once we include their effect, the largest χ_0 contribution comes from the interband zz component associated with the Rashba-split outer FS (Fig. 8b), which can be understood from the Rashba-induced FS spin texture.

While our tight-binding model study captures the salient observations for the (111) KTO 2DEG, it is nevertheless useful to construct a continuum $k{\cdot}p$ theory for the low energy $j=3/2$ states near the Γ-point [34, 35]. This allows us to clearly expose the multipolar character of the magnetic stripe order. We begin with a minimal 3D Luttinger model [24], $H_{\rm bulk}=\alpha_1\sum_i k_i^2\hat{J}_i^2$, with $\alpha_1=0.2\,$eV, which reasonably captures the bulk band dispersion up to a momentum cutoff which we fix as $\Lambda=\pi/3$ (momenta are in units of the inverse cubic lattice constant $1/a$). Here, $\hat{J}_i$ refer to spin-3/2 angular momentum operators (with $i=x,y,z$), and $\hat{J}_0$ denotes the 4×4 identity matrix. To describe the (111) 2DEG, we project to 2D so that

$$H_{2D}^{(0)}=\frac{\alpha_1}{6}\Big[(\sqrt{3}k_1+k_2)^2\hat{J}_x^2+(\sqrt{3}k_1-k_2)^2\hat{J}_y^2+4k_2^2\hat{J}_z^2\Big] \quad (3)$$

with k_1,k_2 being momenta respectively along the $(1\bar{1}0)$ and $(11\bar{2})$ directions. To describe the hexagonal FS, we include the symmetry-allowed sixth-order terms,

$$\begin{aligned}H_{2D}^{(1)}=&\left[\beta_1(k_+^6+k_-^6)+\beta_2(k_+^3+k_-^3)^2\right]\hat{J}_0\\&+\beta_3(k_+^3-k_-^3)^2\hat{J}_3^2\end{aligned} \quad (4)$$

where $\hat{J}_3=(\hat{J}_x+\hat{J}_y+\hat{J}_z)/\sqrt{3}$ and $k_\pm=k_1\pm ik_2$. We set $(\beta_1,\beta_2,\beta_3)=(0.35,0.6,-0.65)\,$eV; although $\{\beta_i\}$ naively appear to be large energy scales, note that $\beta_i k_F^4\ll\alpha_1$ for relevant densities. Finally, we incorporate two weaker terms: a trigonal distortion $\tilde{\Delta}$, and a Rashba coupling $\tilde{\gamma}$ from inversion breaking,

$$H_{2D}^{(2)}=\tilde{\Delta}\hat{J}_3^2+\tilde{\gamma}(\hat{J}_1k_2-\hat{J}_2k_1) \quad (5)$$

where $J_1=\frac{1}{\sqrt{2}}(J_x-J_y)$, $J_2=\frac{1}{\sqrt{6}}(J_x+J_y-2J_z)$, and we fix $(\tilde{\Delta},\tilde{\gamma})=(7,7)\,$meV. Our $k\cdot p$ model for the (111) 2DEG, $H_{\rm 2DEG}=H_{2D}^{(0)}+H_{2D}^{(1)}+H_{2D}^{(2)}$, reasonably reproduces the tight-binding FSs from low to moderate densities [24].

The susceptibility matrix for this $k\cdot p$ model involves the full set of multipole operators constructed from the $j=3/2$ quartet. In addition to dipole operators $\hat{J}_i$, this includes five quadrupoles (triplet: Γ_5, doublet: Γ_3) and seven octupoles (singlet: Γ_2, triplets: Γ_4 and Γ_5); see [24] for the table of operators. We find that the susceptibility restricted to only the dipole operators reproduces the behavior shown in Fig. 4b [24]. Fig. 5a shows the largest eigenvalue of the *full* 15 × 15 matrix susceptibility, for both intraband χ_{11},χ_{22} and interband $\chi_{12}+\chi_{21}$

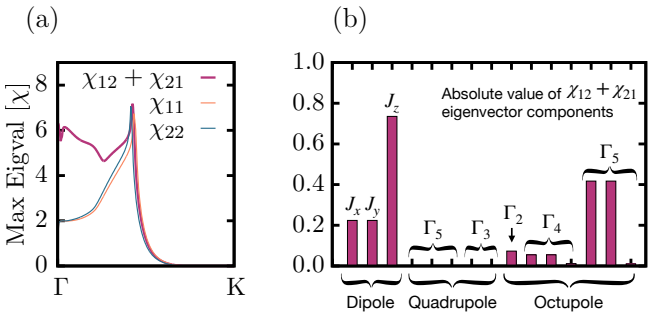


FIG. 5. (a) Maximum eigenvalues of the susceptibility matrix for $j=3/2$ multipoles, showing that the interband instability (thick solid line) slightly dominates over the intraband ones (thin solid lines). (b) Magnitude of the eigenvector components for $\chi_{12}+\chi_{21}$ at $\mathbf{q}_s$ (peak momentum in (a)), showing that the dominant order is composed of intertwined time-reversal breaking dipolar ($\sim J_z$) and octupolar (Γ_5) modulations.

cases, for momentum along the nesting Γ-K direction. The strongest response still occurs for the interband χ between the two spin-split FSs. The key difference is that the intraband χ_{11},χ_{22} also show strongly enhanced, but nevertheless subdominant, peaks. Fig. 5b plots the magnitude of the eigenvector components of $\chi_{12}+\chi_{21}$ for the different multipoles at the peak momentum, showing that the symmetry breaking corresponds to intertwined magnetic dipolar and octupolar orders. As a consequence, the 2DEG stripe should exhibit modulated loop currents from octupolar order [36, 37].

We conclude with a discussion of the implications of our work. Given the involvement of EuO, and the fact that a magnetic stripe model gives a more natural explanation for a single-$\mathbf{q}$ state than a charge-only model, we conclude that the 'nematic' phase seen by Liu *et al.* [3] below $T_s\sim 2.2\,$K is a magnetic stripe. Experiments such as linear optical dichroism, Raman scattering, and resonant x-ray diffraction could shed further light on the nature of this broken symmetry state at the interface. The vestigial nematicity associated with the stripe order is expected to have relatively longer range correlations [38, 39], so it is likely to be pinned by the device geometry. The magnetic stripe state should also strongly impact the SC order. The gapped FS shown in Fig. 3 will reduce the number of states available for pairing, resulting in a lower T_c in samples which exhibit nematicity. In addition, it will cause the SC itself to be anisotropic. Furthermore, for a spin-density wave state, the pairing in a paramagnetic basis can be written as a linear combination of a spin singlet at $\mathbf{Q}=0$ (here, $\mathbf{Q}$ refers to the center of mass momentum of the pair), and one component of a spin triplet at the magnetic wavevector, $\mathbf{Q}=\mathbf{q}_s$ [40]. As such, the superconducting state will also exhibit spatial modulation, similar to a pair density wave state [41], as suggested by Liu *et al.* [3]. A full treatment of the

pairing problem would involve explicitly considering the Rashba splitting, given that its value exceeds both T_s and T_c. Finally, the increase of T_c with carrier density could be due to the suppression of the magnetic stripe phase. This competition is commonly observed in density wave materials such as Cu_xTiSe_2 [42].

The authors thank Anand Bhattacharya, Changjiang Liu and Ivar Martin for discussions. This work was supported by the Materials Sciences and Engineering Division, Basic Energy Sciences, Office of Science, U. S. Dept. of Energy. AP acknowledges funding from NSERC of Canada.

[1] N. Reyren, S. Thiel, A. D. Caviglia, L. F. Kourkoutis, G. Hammerl, C. Richter, C. W. Schneider, T. Kopp, A.-S. Rüetschi, D. Jaccard, M. Gabay, D. A. Muller, J.-M. Triscone, and J. Mannhart, Science **317**, 1196 (2007).
[2] K. Ueno, S. Nakamura, H. Shimotani, H. Yuan, N. Kimura, T. Nojima, H. Aoki, Y. Iwasa, and M. Kawasaki, Nature Nanotechnology **6**, 408 (2011).
[3] C. Liu, X. Yan, D. Jin, Y. Ma, H.-W. Hsiao, Y. Lin, T. M. Bretz-Sullivan, X. Zhou, J. Pearson, B. Fisher, *et al.*, arXiv preprint arXiv:2004.07416 (2020).
[4] Y. Ando, K. Segawa, S. Komiya, and A. N. Lavrov, Phys. Rev. Lett. **88**, 137005 (2002).
[5] V. Hinkov, D. Haug, B. Fauqué, P. Bourges, Y. Sidis, A. Ivanov, C. Bernhard, C. T. Lin, and B. Keimer, Science **319**, 597 (2008).
[6] J. Paglione and R. L. Greene, Nature Physics **6**, 645 (2010).
[7] K. Matano, M. Kriener, K. Segawa, Y. Ando, and G.-q. Zheng, Nature Physics **12**, 852 (2016).
[8] S. Yonezawa, K. Tajiri, S. Nakata, Y. Nagai, Z. Wang, K. Segawa, Y. Ando, and Y. Maeno, Nature Physics **13**, 123 (2017).
[9] M. Hecker and J. Schmalian, npj Quantum Materials **3**, 1 (2018).
[10] Y. Cao, D. Rodan-Legrain, J. M. Park, F. N. Yuan, K. Watanabe, T. Taniguchi, R. M. Fernandes, L. Fu, and P. Jarillo-Herrero, arXiv preprint arXiv:2004.04148 (2020).
[11] L. F. Mattheiss, Phys. Rev. B **6**, 4718 (1972).
[12] F. Y. Bruno, S. McKeown Walker, S. Ricc, A. de la Torre, Z. Wang, A. Tamai, T. K. Kim, M. Hoesch, M. S. Bahramy, and F. Baumberger, Advanced Electronic Materials **5**, 1800860 (2019).
[13] L. Fu, Phys. Rev. Lett. **115**, 026401 (2015).
[14] J. W. Harter, Z. Y. Zhao, J.-Q. Yan, D. G. Mandrus, and D. Hsieh, Science **356**, 295 (2017).
[15] S. Di Matteo and M. R. Norman, Phys. Rev. B **96**, 115156 (2017).
[16] S. Hayami, Y. Yanagi, H. Kusunose, and Y. Motome, Phys. Rev. Lett. **122**, 147602 (2019).
[17] G. E. Jellison, I. Paulauskas, L. A. Boatner, and D. J. Singh, Phys. Rev. B **74**, 155130 (2006).
[18] H. Nakamura and T. Kimura, Phys. Rev. B **80**, 121308 (2009).
[19] P. D. C. King, R. H. He, T. Eknapakul, P. Buaphet, S.-K. Mo, Y. Kaneko, S. Harashima, Y. Hikita, M. S. Bahramy, C. Bell, Z. Hussain, Y. Tokura, Z.-X. Shen, H. Y. Hwang, F. Baumberger, and W. Meevasana, Phys. Rev. Lett. **108**, 117602 (2012).
[20] A. F. Santander-Syro, C. Bareille, F. Fortuna, O. Copie, M. Gabay, F. Bertran, A. Taleb-Ibrahimi, P. Le Fèvre, G. Herranz, N. Reyren, M. Bibes, A. Barthélémy, P. Lecoeur, J. Guevara, and M. J. Rozenberg, Phys. Rev. B **86**, 121107 (2012).
[21] H. Zhang, X. Yan, X. Zhang, S. Wang, C. Xiong, H. Zhang, S. Qi, J. Zhang, F. Han, N. Wu, B. Liu, Y. Chen, B. Shen, and J. Sun, *ACS Nano*, ACS Nano **13**, 609 (2019).
[22] C. Bareille, F. Fortuna, T. Rödel, F. Bertran, M. Gabay, O. H. Cubelos, A. Taleb-Ibrahimi, P. Le Fevre, M. Bibes, A. Barthélémy, *et al.*, Scientific Reports **4**, 3586 (2014).
[23] D. Xiao, W. Zhu, Y. Ran, N. Nagaosa, and S. Okamoto, Nature Communications **2**, 1 (2011).
[24] See the Supplemental Material for details of the (i) bilayer tight-binding model, (ii) symmetry analysis leading to $k \cdot p$ model and its Fermi surfaces, table of multipolar operators, and additional susceptibility plots.
[25] G. Khalsa, B. Lee, and A. H. MacDonald, Phys. Rev. B **88**, 041302 (2013).
[26] These two bands refer to the lowest subset of bands in quantum well language. There is weak evidence from ARPES for higher level sub-bands, but as these are over 100 meV higher in energy, they play no role in regards to the low energy physics discussed here.
[27] J. Desclaux, Atomic data and nuclear data tables **12**, 311 (1973).
[28] H. Zhang, Y. Yun, X. Zhang, H. Zhang, Y. Ma, X. Yan, F. Wang, G. Li, R. Li, T. Khan, Y. Chen, W. Liu, F. Hu, B. Liu, B. Shen, W. Han, and J. Sun, Phys. Rev. Lett. **121**, 116803 (2018).
[29] The Zeeman splittings of $\epsilon_{k,n}$ were not included in the calculations. Also note that in Figs. 2c and 4b, we plot the diagonal elements of the 3 by 3 spin matrix. We find this diagonal approximation is a good one for the maximum (i.e., zz) eigenvalue. Moreover, in Fig. 2c, an implicit sum has been done over the Kramers degeneracy. That is 11 stands for 11+12+21+22, etc.
[30] M. R. Norman, A. Kanigel, M. Randeria, U. Chatterjee, and J. C. Campuzano, Phys. Rev. B **76**, 174501 (2007).
[31] W. L. McMillan, Phys. Rev. B **12**, 1187 (1975).
[32] A. Melikyan and M. R. Norman, Phys. Rev. B **89**, 024507 (2014).
[33] N. Boudjada, G. Wachtel, and A. Paramekanti, Phys. Rev. Lett. **120**, 086802 (2018).
[34] J. M. Luttinger, Phys. Rev. **102**, 1030 (1956).
[35] J. W. F. Venderbos, L. Savary, J. Ruhman, P. A. Lee, and L. Fu, Phys. Rev. X **8**, 011029 (2018).
[36] A. Paramekanti, D. D. Maharaj, and B. D. Gaulin, Phys. Rev. B **101**, 054439 (2020).
[37] S. Voleti, D. D. Maharaj, B. D. Gaulin, G. Luke, and A. Paramekanti, Phys. Rev. B **101**, 155118 (2020).
[38] L. Nie, A. V. Maharaj, E. Fradkin, and S. A. Kivelson, Phys. Rev. B **96**, 085142 (2017).
[39] R. M. Fernandes, P. P. Orth, and J. Schmalian, Annual Review of Condensed Matter Physics **10**, 133 (2019), https://doi.org/10.1146/annurev-conmatphys-031218-013200.
[40] E. W. Fenton, Progress of Theoretical Physics Supplement **80**, 94 (1984).
[41] D. F. Agterberg, J. S. Davis, S. D. Edkins, E. Fradkin,

D. J. Van Harlingen, S. A. Kivelson, P. A. Lee, L. Radzihovsky, J. M. Tranquada, and Y. Wang, Annual Review of Condensed Matter Physics **11**, 231 (2020).
[42] E. Morosan, H. W. Zandbergen, B. S. Dennis, J. W. G. Bos, Y. Onose, T. Klimczuk, A. P. Ramirez, N. P. Ong, and R. J. Cava, Nature Physics **2**, 544 (2006).
[43] R. Shiina, O. Sakai, H. Shiba, and P. Thalmeier, Journal of the Physical Society of Japan **67**, 941 (1998), https://doi.org/10.1143/JPSJ.67.941.
[44] G. Chen, R. Pereira, and L. Balents, Phys. Rev. B **82**, 174440 (2010).

Tight-binding model

The bilayer model for $KTaO_3$ (KTO) oriented along the (111) direction consists of three orbitals and two layers [23]. Including the spin-orbit coupling, λ, the secular matrix is of order 12. We use the basis $\{|d_{1,yz\uparrow}\rangle, |d_{1,xz\uparrow}\rangle, |d_{1,xy\uparrow}\rangle, |d_{2,yz\uparrow}\rangle, |d_{2,xz\uparrow}\rangle, |d_{2,xy\uparrow}\rangle, |d_{1,yz\downarrow}\rangle, |d_{1,xz\downarrow}\rangle, |d_{1,xy\downarrow}\rangle, |d_{2,yz\downarrow}\rangle, |d_{2,xz\downarrow}\rangle, |d_{2,xy\downarrow}\rangle\}$, where indices $1, 2$ label the layers. For purposes here, we only consider the largest hopping term, t, which is diagonal in the orbital index, but off-diagonal in the layer index. The secular matrix has the following form:

$$\hat{\mathcal{H}}(\boldsymbol{k}) = \begin{pmatrix}
0 & \frac{\Delta}{2}+\frac{i\lambda}{2} & \frac{\Delta}{2} & \xi_1 & 0 & 0 & 0 & 0 & -\frac{\lambda}{2} & 0 & 0 & 0 \\
\frac{\Delta}{2}-\frac{i\lambda}{2} & 0 & \frac{\Delta}{2} & 0 & \xi_2 & 0 & 0 & 0 & \frac{i\lambda}{2} & 0 & 0 & 0 \\
\frac{\Delta}{2} & \frac{\Delta}{2} & 0 & 0 & 0 & \xi_3 & \frac{\lambda}{2} & -\frac{i\lambda}{2} & 0 & 0 & 0 & 0 \\
\xi_1^* & 0 & 0 & 0 & \frac{\Delta}{2}+\frac{i\lambda}{2} & \frac{\Delta}{2} & 0 & 0 & 0 & 0 & 0 & -\frac{\lambda}{2} \\
0 & \xi_2^* & 0 & \frac{\Delta}{2}-\frac{i\lambda}{2} & 0 & \frac{\Delta}{2} & 0 & 0 & 0 & 0 & 0 & \frac{i\lambda}{2} \\
0 & 0 & \xi_3^* & \frac{\Delta}{2} & \frac{\Delta}{2} & 0 & 0 & 0 & 0 & \frac{\lambda}{2} & -\frac{i\lambda}{2} & 0 \\
0 & 0 & \frac{\lambda}{2} & 0 & 0 & 0 & 0 & \frac{\Delta}{2}-\frac{i\lambda}{2} & \frac{\Delta}{2} & \xi_1 & 0 & 0 \\
0 & 0 & \frac{i\lambda}{2} & 0 & 0 & 0 & \frac{\Delta}{2}+\frac{i\lambda}{2} & 0 & \frac{\Delta}{2} & 0 & \xi_2 & 0 \\
-\frac{\lambda}{2} & -\frac{i\lambda}{2} & 0 & 0 & 0 & 0 & \frac{\Delta}{2} & \frac{\Delta}{2} & 0 & 0 & 0 & \xi_3 \\
0 & 0 & 0 & 0 & 0 & \frac{\lambda}{2} & \xi_1^* & 0 & 0 & 0 & \frac{\Delta}{2}-\frac{i\lambda}{2} & \frac{\Delta}{2} \\
0 & 0 & 0 & 0 & 0 & \frac{i\lambda}{2} & 0 & \xi_2^* & 0 & \frac{\Delta}{2}+\frac{i\lambda}{2} & 0 & \frac{\Delta}{2} \\
0 & 0 & 0 & -\frac{\lambda}{2} & -\frac{i\lambda}{2} & 0 & 0 & 0 & \xi_3^* & \frac{\Delta}{2} & \frac{\Delta}{2} & 0
\end{pmatrix}. \tag{6}$$

where we define:

$$\begin{aligned}
\xi_1 &= -te^{ik_2c}\left[1+e^{i\left(\frac{\sqrt{3}k_1c}{2}-\frac{3k_2c}{2}\right)}\right] \\
\xi_2 &= -te^{ik_2c}\left[1+e^{-i\left(\frac{\sqrt{3}k_1c}{2}+\frac{3k_2c}{2}\right)}\right] \\
\xi_3 &= -2t\cos\left(\frac{\sqrt{3}k_1c}{2}\right)e^{-i\frac{k_2c}{2}}.
\end{aligned} \tag{7}$$

Here, $k_1 \equiv k_{[1\bar{1}0]}$ and $k_2 \equiv k_{[11\bar{2}]}$ refer to orthogonal momenta in the hexagonal surface Brillouin zone (BZ), with c being the projection of the bulk lattice constant, a, onto the (111) plane (i.e., $c = \sqrt{2/3}a$ with $a = 3.99$ Å). The in-plane (111) lattice constant is $\sqrt{3}c$, which sets the scale for the surface BZ. We chose $t = -1$ eV which, in the absence of other terms, fixes the total bandwidth of the model to $4|t|$ (the value of t being set by the bulk KTO bandwidth). The SOC term for t_{2g} orbitals has a value of 265 meV, leading to a bare quartet-singlet splitting of 397.5 meV at Γ (i.e., when t is turned off). This value has been chosen to match the large spin-orbit splitting reported from ab initio calculations of KTO [12]. In addition, a small on-site trigonal distortion ($\Delta = 10$ meV) is included that is off-diagonal in the orbital index. With the other terms turned off, this leads to a 15 meV splitting at Γ. We have found that the other (smaller) hoppings, as well as the potential difference between the two layers, which were considered in Ref. 23, play only a minor role and are not included here.

The t-only model generates a Fermi surface consisting of three pairs of parallel lines along each the Γ-M direction (Fig. 6a), which are perfectly nested along Γ-K. Once spin-orbit coupling is included, the band structure changes and the flat band in the t-only model becomes dispersive as seen in Fig. 6b. With this model, we have performed calculations at two densities (set by the chemical potential), a higher one to match the ARPES results [12], and a lower one to match that of Liu *et al.* [3]. These two densities give rise to different Fermi surfaces (Figs. 6c and 6d). For the higher density, the outer

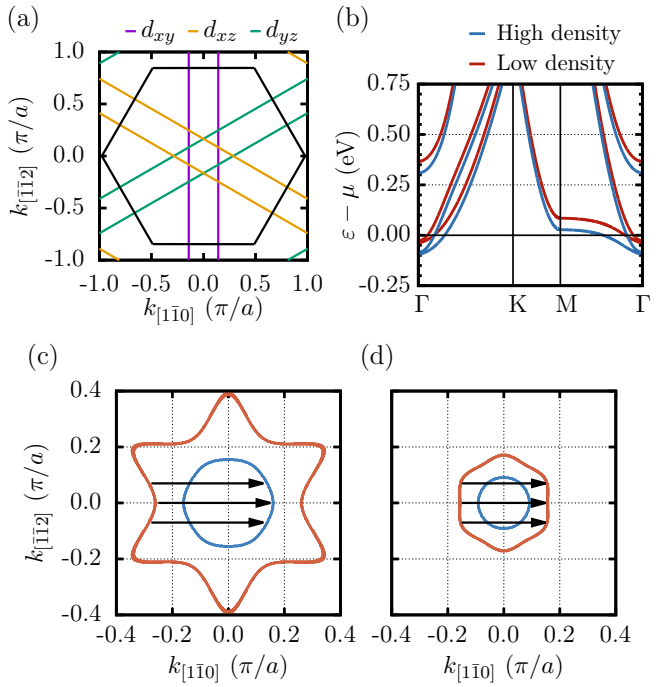


FIG. 6. (a) Fermi surface of (111) KTO in a t-only bilayer model, with Γ-K along the horizontal axis and Γ-M along the vertical axis. The bands are labeled by their t_{2g} content, and the hexagon marks the surface Brillouin zone boundary. (b) Electronic band structure including spin-orbit coupling and a small trigonal distortion. The two sets of curves correspond to two chemical potentials adjusted to match the carrier densities reported by Bruno *et al.* [12] (high density) and Liu *et al.* [3] (low density). Fermi surface for (c) the high density case and (d) the low density case. The horizontal arrows indicate the nestings along Γ-K that were identified by the susceptibility.

pocket has a star-like shape and the inner pocket has a hexagonal shape. In this case, the maximum in the susceptibility does not come along Γ-M (due to nesting of the outer star surface), but rather along Γ-K due to nesting between the outer and inner surfaces. However, in the lower density case, the outer surface becomes hexagonal, and the maximum in the susceptibility is due to nesting along Γ-K for the outer surface, as shown in the main text.

Rashba Term

The Rashba term can be derived by generalizing the work of Khalsa *et al.* [25] to the (111) case. As (111) is parallel to $x+y+z$, more terms enter than in their (001) case. As an example, the yz to xy hopping along the Ta-O-Ta cubic z direction is of the form $\langle yz|\, y\rangle \langle y|\, E_x\, |xy\rangle$ where the first matrix element is $+t_{pd}$, with t_{pd} the overlap integral between Ta $5d$ and O $2p$ orbitals, and the second one is the inversion breaking term due to the electric field along the x direction, E_x. This results in the following matrix elements, γ, to be added to the secular matrix:

$$\begin{aligned}\gamma_{1yz,2xz} &= 2it_R \sin\left(\frac{\sqrt{3}k_1 c}{2}\right) e^{-i\frac{k_2 c}{2}} \\ \gamma_{1yz,2xy} &= t_R e^{ik_2 c}\left[1 - e^{-i\left(\frac{\sqrt{3}k_1 c}{2}+\frac{3k_2 c}{2}\right)}\right] \\ \gamma_{1xz,2xy} &= t_R e^{ik_2 c}\left[1 - e^{i\left(\frac{\sqrt{3}k_1 c}{2}-\frac{3k_2 c}{2}\right)}\right]\end{aligned} \tag{8}$$

where diagonality in the spin index is implicit. (Note that this corresponds to an orbital inversion symmetry breaking and is thus spin-diagonal.) The spin-splitting arises from the combination of this inversion breaking term and the atomic SOC. We have found that a value of t_R of 2 meV is needed to reproduce the suggested Rashba splitting along Γ-K of Bruno *et al.* [12]. This value leads to an almost uniform splitting of around $0.005\pi/c$ for the outer surface of the lower density case of Liu *et al.* [3].

j=3/2 effective model and multipoles

For a cubic crystal, the symmetry-allowed continuum 4-band Luttinger model for the 3D bulk dispersion near the Γ-point is given, to $\mathcal{O}(k^2)$, by

$$H_{3D}^{\text{Lutt}} = \alpha_1 k^2 \hat{J}_0 + \alpha_2 (\mathbf{k}\cdot\hat{\mathbf{J}})^2 + \alpha_3 \sum_{i=x,y,z} k_i^2 \hat{J}_i^2 \tag{9}$$

Here, $\hat{J}_i$ refer to spin-3/2 angular momentum operators (with $i = x, y, z$), $\hat{J}_0$ is the 4×4 identity matrix, and we measure momenta in units of $1/a$ where $a \approx 4$Å is the cubic lattice constant. For $KTaO_3$, we find that a single parameter model, with $\alpha_1 = \alpha_2 = 0$ and $\alpha_3 = 0.2$ eV, captures the band dispersion near the Γ point. We impose a momentum cutoff $\Lambda = \pi/3$.

To describe the (111) 2DEG, we take this dispersion and project it to 2D, expressing it in terms of orthogonal momentum components in the plane of the 2DEG, namely k_1 and k_2 which are respectively along the $(1\bar{1}0)$ and $(11\bar{2})$ directions, so $k_x = (k_2 + \sqrt{3}k_1)/\sqrt{6}$, $k_y = (k_2 - \sqrt{3}k_1)/\sqrt{6}$, and $k_z = -2k_2/\sqrt{6}$. The projected 2D Hamiltonian is

$$H_{2D}^{(0)} = \alpha_3\left[\frac{(\sqrt{3}k_1+k_2)^2}{6}\hat{J}_x^2 + \frac{(\sqrt{3}k_1-k_2)^2}{6}\hat{J}_y^2 + \frac{2k_2^2}{3}\hat{J}_z^2\right] \tag{10}$$

Going beyond these terms which descend from the bulk dispersion, we need to incorporate additional symmetry allowed terms in order to describe the 2DEG dispersion. We begin by considering mirror symmetry M_1, time reversal $\mathcal{T}$, three-fold rotation $\mathcal{R}_{2\pi/3}$, and inversion $\mathcal{I}$, and then incorporate Rashba terms from breaking $\mathcal{I}$. For

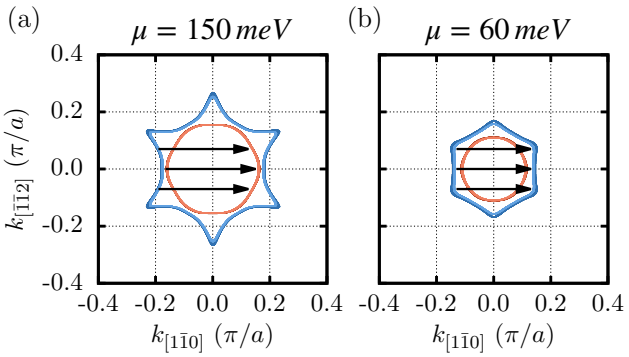


FIG. 7. Fermi surfaces for the 2DEG upon including the Rashba SOC and trigonal distortion, shown for chemical potential $\mu = 150\,\text{meV}$ ($n \approx 6.5 \times 10^{13}/\text{cm}^2$) and $\mu = 60\,\text{meV}$ ($n \approx 3.5\times10^{13}/\text{cm}^2$). In each case, the spin-split FSs are more clearly visible for the outer pair of bands, with the splitting being slightly more significant along the $k_2 \equiv k_{[\bar{1}\bar{1}2]}$ direction which corresponds to the Γ-M direction.

convenience, we define $k_\pm = k_1 \pm ik_2$. Under lattice symmetry operations, the momenta and $\vec{J}$ transform as:

$$\begin{aligned} M_1 &: \begin{cases} (k_1,k_2) & \to\ (-k_1,k_2) \\ (J_x,J_y,J_z) & \to\ (-J_y,-J_x,-J_z) \end{cases} \\ R_{2\pi/3} &: \begin{cases} k_\pm & \to\ k_\pm e^{\pm i2\pi/3} \\ (J_x,J_y,J_z) & \to\ (J_y,J_z,J_x) \end{cases} \\ \mathcal{I} &: \begin{cases} (k_1,k_2) & \to\ (-k_1,-k_2) \\ (J_x,J_y,J_z) & \to\ (J_x,J_y,J_z) \end{cases} \end{aligned} \tag{11}$$

If inversion and time-reversal are unbroken, cubic terms in the momenta are ruled out, and the next important terms which we find capture the hexagonal shape of the 2DEG dispersion are sixth order terms in momenta,

$$\begin{aligned} H_{2D}^{(1)} = &\left[\beta_1(k_+^6+k_-^6)+\beta_2(k_+^3+k_-^3)^2\right]\hat{J}_0 \\ &+\beta_3(k_+^3-k_-^3)^2\hat{J}_3^2 \end{aligned} \tag{12}$$

where $\hat{J}_3 = (\hat{J}_x+\hat{J}_y+\hat{J}_z)/\sqrt{3}$. Finally, we incorporate two weaker terms: an effective trigonal distortion $\tilde{\Delta}$, and a Rashba coupling $\tilde{\gamma}$ from inversion breaking, via

$$H_{2D}^{(2)} = \tilde{\Delta}\hat{J}_3^2 + \tilde{\gamma}(\hat{J}_1k_2 - \hat{J}_2k_1) \tag{13}$$

where $J_1 = (J_x - J_y)/\sqrt{2}$ and $J_2 = (J_x + J_y - 2J_z)/\sqrt{6}$. We set $(\beta_1,\beta_2,\beta_3) = (0.35, 0.6, -0.65)\,\text{eV}$, and fix the weaker terms to be $(\tilde{\Delta},\tilde{\gamma}) = (7,7)\,\text{meV}$ in order to match the tight-binding results for the spin splitting of the FSs and the splitting of the $j = 3/2$ quartet at the Γ-point. This Hamiltonian $H_{2\text{DEG}} = H_{2D}^{(0)} + H_{2D}^{(1)} + H_{2D}^{(2)}$ may be viewed as a simple continuum $j = 3/2$ model for the $KTaO_3$ (111) 2DEG for low to moderate dopings. The Fermi surfaces from this $k\cdot p$ Hamiltonian are shown in Fig. 7, and are in reasonable agreement with the FSs from the tight-binding model discussed in the main text.

The multipole moments within the $j = 3/2$ quartet are given in the table below. We have normalized these multipole operators such that $\text{Tr}(\mathcal{M}_\alpha^2) = 4j(j+1)/3$. This normalization is chosen such that the dipole operator matrices are simply the usual $\hat{J}_i$ matrices. Different normalization schemes, as in Refs. 43 and 44, would lead to quantitative changes in the susceptibility results in the main text, but the key conclusions, that the dominant eigenvalue of χ stems from interband (12+21) nesting, and that it involves dipoles and octupoles, remains robust.

Multipole	Symmetry	Operator
Dipole	Γ_4	$\mathcal{M}_x = J_x$
		$\mathcal{M}_y = J_y$
		$\mathcal{M}_z = J_z$
Quadrupole	Γ_5	$\mathcal{M}_{yz} = \sqrt{\frac{5}{12}}\overline{J_yJ_z}$
		$\mathcal{M}_{xz} = \sqrt{\frac{5}{12}}\overline{J_xJ_z}$
		$\mathcal{M}_{xy} = \sqrt{\frac{5}{12}}\overline{J_xJ_y}$
	Γ_3	$\mathcal{M}_{x^2-y^2} = \sqrt{\frac{5}{12}}(J_x^2 - J_y^2)$
		$\mathcal{M}_{3z^2} = \sqrt{\frac{5}{36}}(3J_z^2 - J(J+1))$
Octupole	Γ_2	$\mathcal{M}_{xyz} = \sqrt{\frac{5}{27}}\overline{J_xJ_yJ_z}$
	Γ_4	$\mathcal{M}_x^\alpha = \frac{2}{3}(J_x^3 - \frac{1}{2}(\overline{J_xJ_y^2} + \overline{J_xJ_z^2}))$
		$\mathcal{M}_y^\alpha = \frac{2}{3}(J_y^3 - \frac{1}{2}(\overline{J_yJ_x^2} + \overline{J_yJ_z^2}))$
		$\mathcal{M}_z^\alpha = \frac{2}{3}(J_z^3 - \frac{1}{2}(\overline{J_zJ_x^2} + \overline{J_zJ_y^2}))$
	Γ_5	$\mathcal{M}_x^\beta = \sqrt{\frac{5}{27}}\overline{J_x(J_y^2 - J_z^2)}$
		$\mathcal{M}_y^\beta = \sqrt{\frac{5}{27}}\overline{J_y(J_z^2 - J_x^2)}$
		$\mathcal{M}_z^\beta = \sqrt{\frac{5}{27}}\overline{J_z(J_x^2 - J_y^2)}$

TABLE I. The overline symbol indicates a sum over all the possible permutations of the operators, $\overline{J_xJ_z^2} = J_xJ_z^2 + J_zJ_xJ_z + J_z^2J_x$. This table is adapted from Refs. 43 and 44 but with modified normalization.

In order to compare these results with the results from the tight-binding model calculations, we also plot in Fig. 8 the susceptibility eigenvalues for intraband and interband orders when we truncate the susceptibility matrix to just the dipole operators, where we find qualitative agreement with the results from Fig. 4 of the main text.

Fig. 9a-f shows the real and imaginary components of the eigenvectors corresponding to the peaks in χ shown in the main text where we diagonalize the full 15×15 susceptibility matrix.

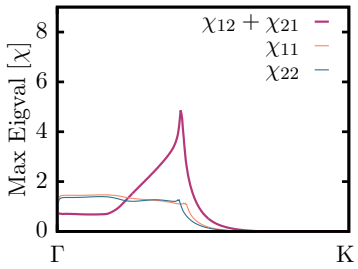


FIG. 8. Largest eigenvalues of the 3×3 susceptibility matrix truncated to just the dipole operators plotted as a function of momentum along Γ-K.

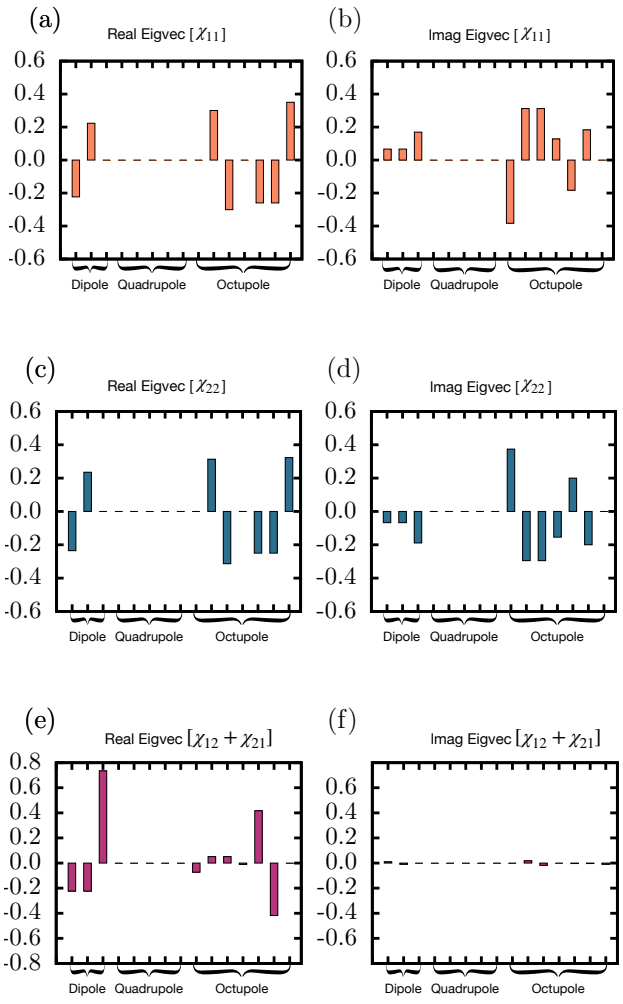


FIG. 9. Real and imaginary components of the dominant eigenvector corresponding to the peaks in χ for (a,b) intraband χ_{11}, (c,d) intraband χ_{22}, and (e,f) interband $\chi_{12} + \chi_{21}$. For the leading instability which corresponds to an interband order, the symmetry breaking pattern involves time-reversal breaking dipolar and octupolar modulations.